Predicted Pressure-Induced High-Energy-Density Iron Pentazolate Salts

Chuli Sun(孙矗丽)[2], Wei Guo(郭伟)[1,2,3*], and Yugui Yao(姚裕贵)[1,2,3]

[1]*Frontiers Science Center for High Energy Material (MOE), Beijing Institute of Technology, Beijing 100081, China*
[2]*Key Laboratory of Advanced Optoelectronic Quantum Architecture and Measurement (MOE), School of Physics, Beijing Institute of Technology, Beijing 100081, China*
[3]*State Key Laboratory of Explosion Science and Technology, Beijing Institute of Technology, Beijing 100081, China*

(Received 26 April 2022; accepted manuscript online 6 July 2022)

Metal-pentazolate compounds as candidates for novel high-energy-density materials have attracted extensive attention in recent years. However, dehydrated pentazolate salts of transition metal iron are rarely reported. We predict two new iron pentazolate salts $Fdd2$-FeN_{10} and $P\bar{1}$(No.1)-FeN_{10} using a constrained crystal search method based on first-principles calculations. We propose that the stable $Fdd2$-FeN_{10} crystal may be synthesized from FeN and N_2 above 20 GPa, and its formation enthalpy is lower than the reported iron pentazolate salt (marked as $P\bar{1}$(No.2)-FeN_{10}). Crystal $P\bar{1}$(No.1)-FeN_{10} is composed of iron bispentazole molecules. Formation enthalpy, phonon spectrum and *ab initio* molecular dynamics calculations are performed to show their thermodynamic, mechanical and dynamic properties. Moreover, the high energy density (3.709 kJ/g, 6.349 kJ/g) and good explosive performance indicate their potential applications as high-energy-density materials.

DOI: 10.1088/0256-307X/39/8/087101

Dinitrogen is one of the most inert gases under ambient conditions due to its strong bond energy (N≡N, ∼954 kJ/mol), while the bond energy of N–N (∼160 kJ/mol) or N=N (∼418 kJ/mol) is weaker. Therefore, a large amount of energy is released when a single bond (double bond) transforms into a triple bond. Polymeric nitrogen containing single or double bonds has been extensively studied by researchers as an eco-friendly new energetic material, among which the pentazolate anion (*cyclo*-N_5^-) has attracted wide attention due to its potential applications in high-energy-density materials (HEDM).

Previous research achievements of pentazolate anion (*cyclo*-N_5^-) are mainly the synthesis of metal or metal-free pentazolate hydrates under ambient conditions, such as $[Mg(H_2O)_6(N_5)_2]\cdot 4H_2O$, $[Na(H_2O)(N_5)_2]\cdot 2H_2O$, $[M(H_2O)_4(N_5)_2]\cdot 4H_2O$ (M = Fe, Co, Zn) and $(N_5)_6(H_3O)_3(NH_4)_4Cl$.[1–4] However, the non-energetic groups (H_2O and Cl) reduce the nitrogen content, energy density and explosive properties of those complexes, making them less interesting in terms of performance. Therefore, the design of stable pentazolate salts that contains fewer non-energetic groups has become a hot-spot in HEDM. In recent years, pentazolate salts containing alkali metals, alkaline earth metals, trivalent metals and transition metals have been discovered through high-pressure experiments or theoretical predictions.[5–15] Transition metal element iron, as the second most common metal element in nature, has a moderate atomic mass and can also provide more electrons. However, the related research on dehydrated iron pentazolate salt is rarely reported. The coordination form of iron with the pentazolate anion (*cyclo*-N_5^-) and the energetics of iron pentazolate salts have intrigued us to investigate their potential synthesis condition, stability and detonation performance.

In this work, through a constrained crystal search combined with density functional theory (DFT) calculations, we find two FeN_{10} pentazolate salts at 40 GPa, i.e., $Fdd2$-FeN_{10} and $P\bar{1}$(No.1)-FeN_{10}. $Fdd2$-FeN_{10} is more energetically favorable than the reported iron pentazolate structure $P\bar{1}$(No.2)-FeN_{10}. Their stability is confirmed by formation enthalpies, phonon spectrum and *ab initio* molecular dynamics (AIMD) simulations. The research of electronic structure and energetics reveals that $Fdd2$-FeN_{10} and $P\bar{1}$(No.1)-FeN_{10} are semiconductors and insulators with high energy density (3.709 kJ/g, 6.349 kJ/g), respectively. Moreover, their better explosive properties also make them good candidates in the field of high-energy powerful explosives.

Computational Methods. Structural predictions were performed by the CALYPSO code, which is an efficient structure prediction method based on particle swarm optimization algorithm to achieve the global or local minimizations in the potential energy surface.[16–18] In our structure search, the *cyclo*-N_5^- is constrained as a unit of the initial structure, and the stoichiometric $Fe_2(N_5)_4$ is used to directly search for thermodynamically stable structures under 40 GPa. During the structure search, first-principles calculations were performed in the framework of DFT to obtain the total energy of the systems, as implemented in the Vienna *ab initio* simulation package (VASP).[19] The electron exchange-correlation effects were described by the Perdew–Burke–Ernzerhof generalized gradient approxima-

*Corresponding author. Email: weiguo7@bit.edu.cn
© 2022 Chinese Physical Society and IOP Publishing Ltd

tion (GGA).[20] The projector-augmented wave method[21] was adopted, and $3d^74s^1$ and $2s^22p^3$ were treated as valence electrons of Fe and N, respectively. In structural optimization, a cut-off energy of 600 eV and a force convergence of 0.02 eV·Å^{-1} were set. Since the optimized ground state structures are non-magnetic, we did not consider the magnetic properties of iron pentazolate salts in subsequent calculations. Meanwhile, the van der Waals interaction was included by using the PBE-D3 method.[22] The effects of PBE-D3 and optB88-vdW[23] methods on crystal energy are shown in Fig. S1 of the Supplemental Material.

In order to study the mechanical stability of the structure, phonon dispersion calculations were performed in the PHONOPY code using the density functional perturbation theory.[24] *Ab initio* molecular dynamics (AIMD) simulations with the NPT ensemble can reflect the dynamic stability of structures under different pressures and temperatures, in which $1 \times 1 \times 2$ (176 atoms) and $3 \times 2 \times 2$ (132 atoms) supercells of *Fdd*2-FeN_{10} and $P\bar{1}$(No.1)-FeN_{10} were used, respectively. The AIMD simulation time at each temperature was set to 10 ps with a step size of 1 fs. The formation enthalpy of iron pentazolate salts relative to solid Fe and N was calculated by the formula $\Delta H_f = [H((FeN_{10})_x) - xH(Fe) - 5xH(N_2)]/11x$ to characterize the thermodynamic stability of structures, in which bcc-Fe, hcp-Fe, α-N_2, $P4_12_12$-N_2 and cg-N[25] are taken as the reference states in the corresponding pressures. Fe–N structures in Fig. 2(a) except the FeN_{10} phase are obtained from the work of Jiao *et al.*,[26] and their enthalpies were recalculated in Fig. 2(a). Energy density is of great significance in the study of energetic materials. When $(FeN_{10})_x$ is decomposed into $F\bar{4}3m$-FeN[27] and dinitrogen gas under ambient conditions, the released energy density E_d was calculated by the following formula $E_d = [E((FeN_{10})_x) - E(xFeN) - E(\frac{9}{2}xN_2)]/x(55.8+140)$, where the energy of dinitrogen gas is ∼0.25 eV/atom lower than α-N_2.[11,28]

Results and Discussion—Crystal Structures and Stability. Through the restrained crystal search, we focus on two FeN_{10} compounds, namely *Fdd*2-FeN_{10} and $P\bar{1}$(No.1)-FeN_{10}, as shown in Fig. 1. Their lattice parameters and atomic positions under ambient conditions can be seen in Table S1 of the Supplemental Material. From Fig. 1(a), we can see that each iron atom forms an octahedral configuration with its neighboring nitrogen atoms, and the N–N bond length of η^3-N_5 ring is around 1.32 Å, which is between the N–N single bond (1.45 Å) and the N=N double bond (1.25 Å). Here, η^n shows the coordination mode of the *cyclo*-N_5^- ligand and the metal atom, where n represents the hapticity of the *cyclo*-N_5^-. Figure 1(b) shows a metallocene-like crystal structure with atomic coordination quite different from *Fdd*2-FeN_{10}, where each iron atom is located between two parallel N_5 rings, and the N–N bond length is ∼1.38 Å. The Fe–N bond length of *Fdd*2-FeN_{10} and $P\bar{1}$(No.1)-FeN_{10} is about 1.96–2.00 Å. Compared with the bond length of Fe–N in $[Fe(H_2O)_4(N_5)_2]\cdot 4H_2O$ (2.17 Å),[4] Fe–N in the two compounds forms a stronger coordination bond. Meanwhile, we also find a crystal structure with space group $P\bar{1}$ which is denoted here as $P\bar{1}$(No.2)-FeN_{10} (Fig. S2), whose local atomic coordination is similar to *Fdd*2-FeN_{10}, but their crystal structures are quite different. The $P\bar{1}$(No.2)-FeN_{10} has also been reported by Huang *et al.*,[29] and its structural information can also be obtained in Table S1 of the Supplemental Material. The three pentazolate salts may undergo phase transition under certain conditions, but phase transition in solid is rather complicated. The LASP software developed by Liu *et al.* may attack this problem by a stochastic surface walking method to predict the crystal phase transition pathway,[30,31] and the research is beyond the scope of this work.

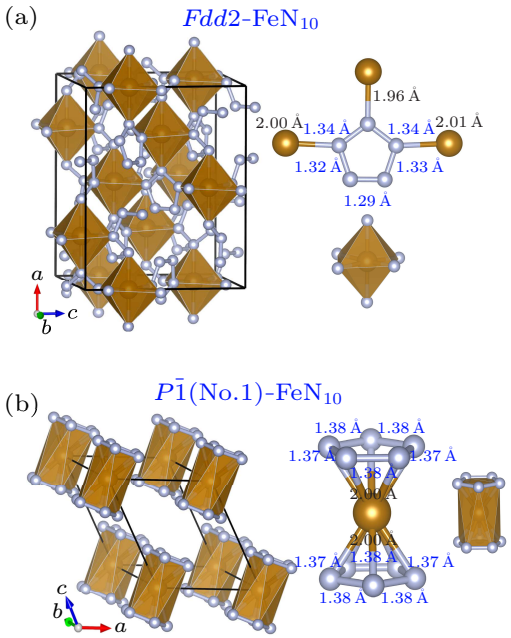

Fig. 1. The crystal structures of (a) *Fdd*2-FeN_{10} and (b) $P\bar{1}$(No.1)-FeN_{10} under ambient pressure. Fe–N and N–N bond lengths are shown in black and blue numbers, respectively.

Formation enthalpy can be used to evaluate the thermodynamic stability of crystal phases, where negative values represent exothermic formation of compounds from elements. Since *Fdd*2-FeN_{10} is more energetically favorable than $P\bar{1}$(No.1)-FeN_{10} and $P\bar{1}$(No.2)-FeN_{10} (Fig. S1), we use *Fdd*2-FeN_{10} for the calculation of formation enthalpy at the Fe:N ratio 1:10. As shown in Fig. 2(a), the convex hulls connect the stable phases by solid lines, and the dashed lines above the solid lines connect the metastable phases. The formation enthalpies of *Fdd*2-FeN_{10} are located on the convex hulls at 30 GPa, 40 GPa, 60 GPa and 70 GPa, respectively, indicating the thermodynamic stability of *Fdd*2-FeN_{10} under high pressure. Figure 2(b) shows that *Fdd*2-FeN_{10} is still the most favorable phase in known FeN_{10} in terms of energy relative to the FeN+4.5N_2 system, and it may be synthesized by $P6_3/mmc$-FeN and $P4_12_12$-N_2 overcoming a certain dynamic barrier at high temperature and > 20 GPa. So, we encourage experimental group to try to synthesize this high-nitrogen content metal nitride since 20 GPa is feasible in many high-pressure devices with large volume.

In order to further evaluate the mechanical and dynamic stability of *Fdd*2-FeN_{10} and $P\bar{1}$(No.1)-FeN_{10}, phonon dispersion curves and AIMD simulations at 0 GPa

and 40 GPa were performed. At 0 GPa, the calculated phonon spectra of $Fdd2$-FeN_{10} and $P\bar{1}$(No.1)-FeN_{10} are shown in Figs. 3(a) and 3(c), respectively. The results for $P\bar{1}$(No.2)-FeN_{10} is also shown in Fig. S3(a) for comparison. The absence of imaginary phonon frequencies indicates their mechanical stability under ambient pressure. It is unsurprising that their mechanical stabilities are improved at 40 GPa, which can be seen in Figs. S4(a), S4(c) and S4(e) of the Supplemental Material.

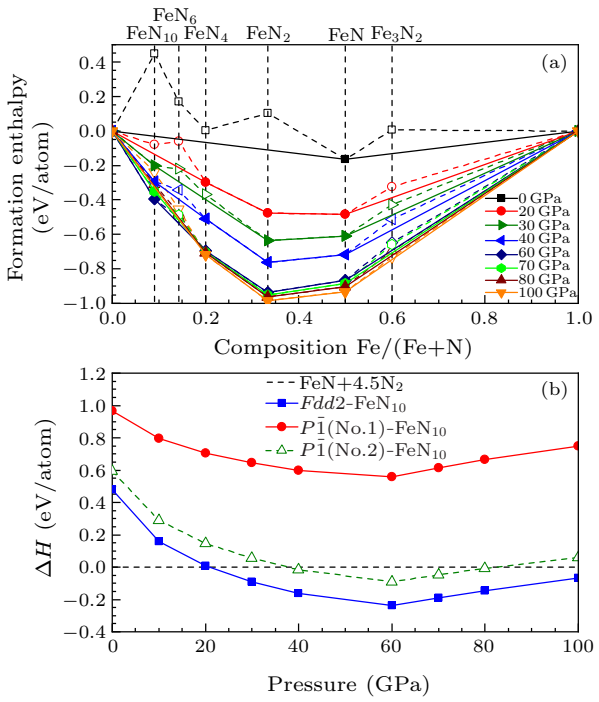

Fig. 2. (a) Formation enthalpies of Fe_xN_y phases with respect to elemental iron and nitrogen solids at different pressures. Except for the FeN_{10} phase, the crystal structures at other ratios are from the work of Jiao *et al.*,[26] and their enthalpies are recalculated. The solid lines connect stable phases, and the dashed lines connect metastable phases. FeN_{10} under different pressures remains $Fdd2$ symmetry, only the volume changes. (b) The enthalpy difference of $Fdd2$-FeN_{10}, $P\bar{1}$(No.1)-FeN_{10} and $P\bar{1}$(No.2)-FeN_{10} relative to the FeN+4.5N_2 system. $F\bar{4}3m$-FeN, $P6_3/mmc$-FeN,[26] α-N_2, $P4_12_12$-N_2 and cg-N[25] are used in the corresponding pressures.

In AIMD simulations, 300 K is used as the initial temperature applied to the crystals, then the structures are heated at 200 K intervals to observe evolutions with increasing temperature. Figures 3(b) and 3(d) reveal that $Fdd2$-FeN_{10} and $P\bar{1}$(No.1)-FeN_{10} can remain stable at about 900 K and 500 K, respectively, under ambient pressure for 10 ps. However, their structures lose stability when the temperature increases to 1000 K and 600 K, which is shown in Fig. S5 of the Supplemental Material. As the temperature rises, the Fe–N bond in $Fdd2$-FeN_{10} breaks first, which is similar to the dynamic characteristics of LiN_5[32] and CuN_5.[13] However, the fracture mode of $P\bar{1}$(No.1)-FeN_{10} is different, where the N_5 ring breaks first with increasing temperature, which is consistent with the pyrolysis mechanism proposed by Zhang *et al.*[33] Under high pressure, the stability of $Fdd2$-FeN_{10} and $P\bar{1}$(No.1)-FeN_{10} is greatly enhanced, and their dynamic stability temperatures are raised to ∼2500 K and ∼800 K, respectively.

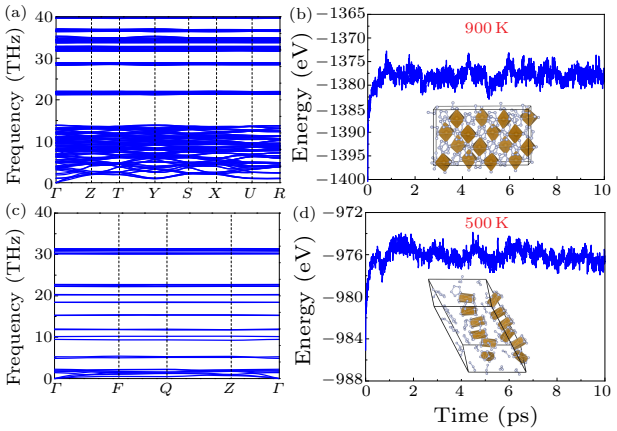

Fig. 3. [(a), (c)] Phonon dispersion curves of $Fdd2$-FeN_{10} and $P\bar{1}$(No.1)-FeN_{10} at 0 GPa. [(b), (d)] Total free energy fluctuations of $Fdd2$-FeN_{10} and $P\bar{1}$(No.1)-FeN_{10} in AIMD simulations. Here, 900 K and 500 K are the highest temperature at which $Fdd2$-FeN_{10} and $P\bar{1}$(No.1)-FeN_{10} can remain stable at ambient pressure respectively, and the illustrations show their structural snapshots after 10 ps.

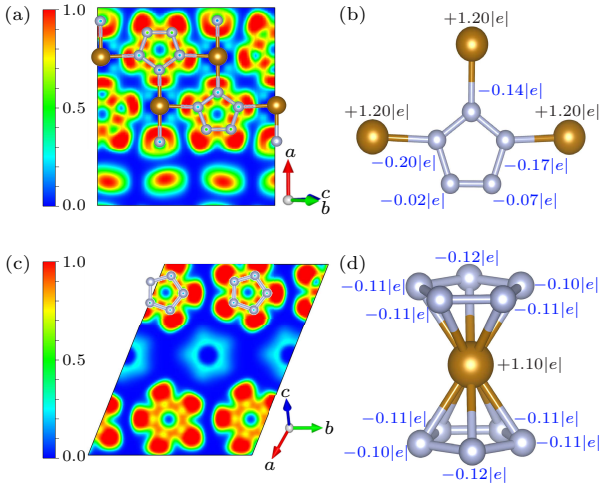

Fig. 4. [(a), (b)] Electron localization function and Bader charge of $Fdd2$-FeN_{10} at 0 GPa, respectively. [(c), (d)] Electron localization function and Bader charge of $P\bar{1}$(No.1)-FeN_{10} at 0 GPa, respectively.

Bond Characteristics. In Order to study the bond characteristics of crystal structures, we calculate and analyze their electron localization function (ELF), charge distribution, and crystal orbital Hamilton population (COHP). The ELF can clearly show their bonding properties, in which the color indicates the possibility of detecting localized electrons. As the color bar changes from blue to red, the detected electrons are more localized. As shown in Figs. 4(a) and 4(c), we can see that there is a strong covalent bond between N atoms in *cyclo*-N_5^-, and a coordination bond between Fe–N of $Fdd2$-FeN_{10}. The coordination bond is a special covalent bond in which the shared electron pair and empty orbital are provided by N atoms and Fe atoms, respectively. Furthermore, we can also see lone-pair electrons existing at the vertex of the

pentagon in *cyclo*-N_5^-. The metal cation and *cyclo*-N_5^- of $P\bar{1}$(No.1)-FeN_{10} involve a π-bond, about half ionic and half covalent, which has been widely reported in the study of iron bispentazole molecule $Fe(\eta^5\text{-}N_5)_2$.[34–36]

Bader charge analysis[37] is used to measure the charge transfer. As shown in Figs. 4(b) and 4(d), iron atoms donate electrons to nitrogen atoms, where the iron atoms in *Fdd*2-FeN_{10} and $P\bar{1}$(No.1)-FeN_{10} have about 1.20e and 1.10e transferred to two N_5 rings, respectively. Moreover, the charge distribution on each N atom in the *cyclo*-N_5^- of $P\bar{1}$(No.1)-FeN_{10} is more homogeneous than that of *Fdd*2-FeN_{10}, indicating that the aromaticity of N_5 rings in $P\bar{1}$(No.1)-FeN_{10} is less disturbed.

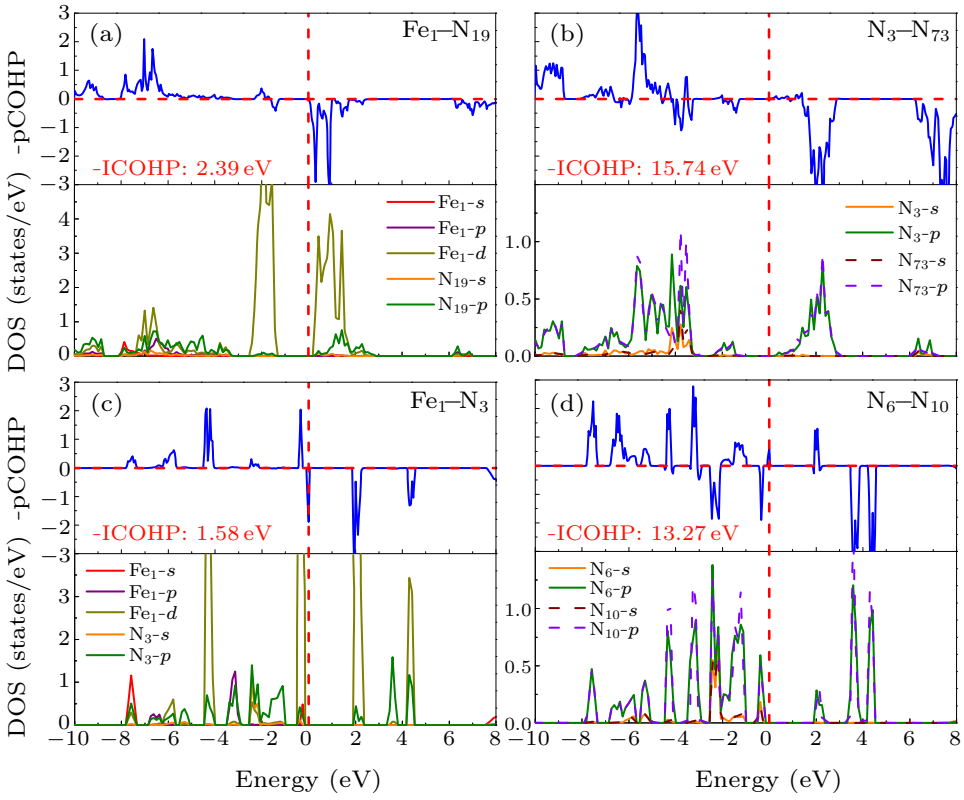

Fig. 5. [(a), (b)] Projected COHP (pCOHP) curves and density of states (DOS) of Fe–N and N–N bonds in *Fdd*2-FeN_{10}. [(c), (d)] Projected COHP (pCOHP) curves and density of states (DOS) of Fe–N and N–N bonds in $P\bar{1}$(No.1)-FeN_{10}. ICOHP denotes integrated COHP.

The COHP[38] can quantitatively characterize the bonding strength of Fe–N and N–N bonds, which is implemented in the LOBSTER program.[39] The –pCOHP (negative projected COHP) is usually employed, with a positive value indicating a bonding state, and a negative value indicating an antibonding state. As shown in Fig. 5, the –pCOHP curves show that the occupied states of Fe–N and N–N bonds in *Fdd*2-FeN_{10} and $P\bar{1}$(No.1)-FeN_{10} are mainly bonding states, only a few occupied states of N–N bonds exist on antibonding orbitals, and the p-wave electrons of nitrogen contribute to the strong covalent bond in *cyclo*-N_5^-. In addition, we also calculate the integrated COHP (ICOHP), which is the energy integral up to the highest occupied energy level. The larger the -ICOHP, the stronger the covalent bonding. From the ICOHP values, we can see that the Fe–N and N–N bonds in *Fdd*2-FeN_{10} have a stronger chemical bond than the corresponding bonds in $P\bar{1}$(No.1)-FeN_{10}. Also, the –ICOHP of N–N bond in *Fdd*2-FeN_{10} is much larger than the Fe–N bond, indicating that the chemical bond of N–N is stronger, which verifies the result of dynamics simulation. Although the –ICOHP of a single Fe–N bond in $P\bar{1}$(No.1)-FeN_{10} is relatively small, the Fe–N bond is not easy to break due to its unique coordination mode, which is also consistent with the MD simulation.

Electronic Structures. Electronic property is essential for the characterization of materials. Here we first focus on electronic band structures and density of states (DOS) of *Fdd*2-FeN_{10} and $P\bar{1}$(No.1)-FeN_{10}. From Fig. 6, we can see that *Fdd*2-FeN_{10} and $P\bar{1}$(No.1)-FeN_{10} show semiconducting nature under ambient pressure with band gaps of 1.592 and 2.192 eV, respectively. Moreover, the partial density of states (pDOS) and partial charges (Fig. S6) intuitively show that the valence band maximum (VBM) and the conduction band minimum (CBM) of *Fdd*2-FeN_{10} and $P\bar{1}$(No.1)-FeN_{10} are mainly contributed by d state of Fe atoms. The distribution of electronic states is mainly related to the atomic coordination mode in the crystal structure. Under the action of crystal field, due to the negative charge of the N atom, all d electrons are subject to its Coulomb repulsion, resulting in the splitting of degenerate electronic states in the d level. As shown in Fig. S7, the octahedral configuration formed by central ion Fe and neighboring N atoms in *Fdd*2-FeN_{10} makes the

VBM mainly composed of dz^2 and dx^2-y^2 electrons, while the CBM mainly from the dyz orbital of Fe atoms. The VBM of $P\bar{1}$(No.1)-FeN_{10} is mainly contributed by the dz^2 state, and the CBM is mainly derived from the dyz and dxz orbitals. It is worth noting that GGA or LDA functionals usually underestimate the band gap, while the GW method [40] has a more reliable description of the band gap of semiconductors and insulators. [41,42] The band gaps of $Fdd2$-FeN_{10} and $P\bar{1}$(No.1)-FeN_{10} are calculated to be 2.573 and 4.913 eV using the GW method, so $P\bar{1}$(No.1)-FeN_{10} should exhibit insulating behavior under ambient pressure.

Meanwhile, the pressure dependence of band gaps is also an important electronic property. The band gap of $P\bar{1}$(No.1)-FeN_{10} decreases as the pressure increases, and the pDOS can be seen in Fig. S8 of the Supplemental Material. Significantly, the band gap of $Fdd2$-FeN_{10} increases with the compression at 0–10 GPa. By comparing and analyzing the pDOS of $Fdd2$-FeN_{10} under different pressures [Fig. 7(b)], we infer that the enhanced coupling between Fe–N and the covalency of N atoms lead to the enhancement of electronic localization, which in turn leads to an increase in the band gap at 0–10 GPa. The trend of band gap increasing with compression is also found in the NeN_{10} and NeN_{22} systems. [43] The pDOS of $Fdd2$-FeN_{10} at 20–100 GPa are also included in Fig. S9 of the Supplemental Material.

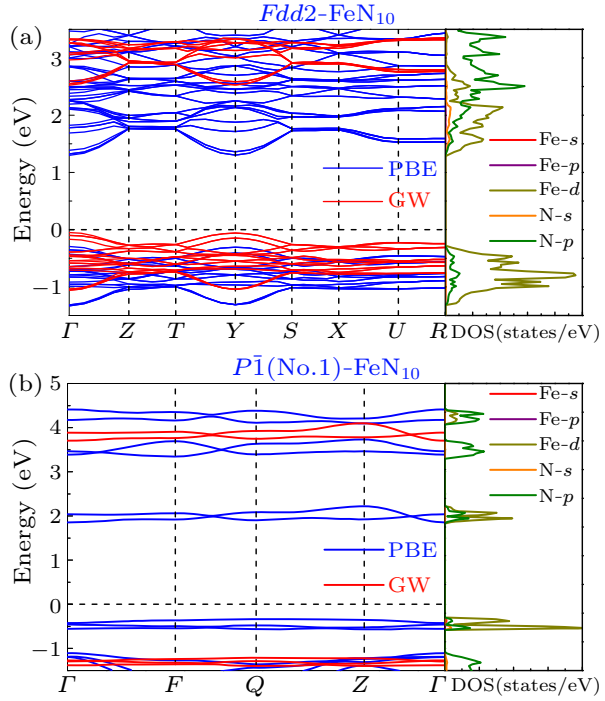

Fig. 6. (a) Band structures and the partial density of states of $Fdd2$-FeN_{10} at 0 GPa. (b) Band structures and the partial density of states of $P\bar{1}$(No.1)-FeN_{10} at 0 GPa.

Explosive Performance. For energetic materials, energy density and detonation properties are key parameters to characterize their performance. As shown in Table 1, when the decomposition products of $Fdd2$-FeN_{10} and $P\bar{1}$(No.1)-FeN_{10} are FeN and N_2(g) under ambient conditions, their energy densities E_d are calculated to be 3.709 kJ/g and 6.349 kJ/g, respectively, and the value of $P\bar{1}$(No.1)-FeN_{10} exceeds the standard energetic material TNT (2,4,6-trinitrotoluene) and HMX (cyclotetramethylene tetranitramine). [27] In addition, the calculated gravimetric energy densities ρ (3.211 g/cm^3, 2.197 g/cm^3) are also higher than TNT and HMX. [44]

Detonation velocity and detonation pressure are two important parameters for designing high-performance explosives. Therefore, we calculate the detonation velocity D and detonation pressure P of $Fdd2$-FeN_{10} and $P\bar{1}$(No.1)-FeN_{10} through the popular empirical Kamlet–Jacobs equations. [44] In the formulas $D = 1.01(NM^{0.5}E_d^{0.5})^{0.5}(1+1.30\rho)$ and $P = 15.58\rho^2NM^{0.5}E_d^{0.5}$, N is the moles of gas produced per gram of compounds, and M is the molar mass of gas products. Table 1 shows that the detonation velocity (14.220 km/s, 12.119 km/s) and detonation pressure (1189.372 kbar, 728.108 kbar) of $Fdd2$-FeN_{10} and $P\bar{1}$(No.1)-FeN_{10} are much higher than those of HMX and TNT, [10,11,44] and the D and P of $Fdd2$-FeN_{10} are even about 2–3 times of TNT and HMX, indicating the potential applications of $Fdd2$-FeN_{10} and $P\bar{1}$(No.1)-FeN_{10} in high explosives.

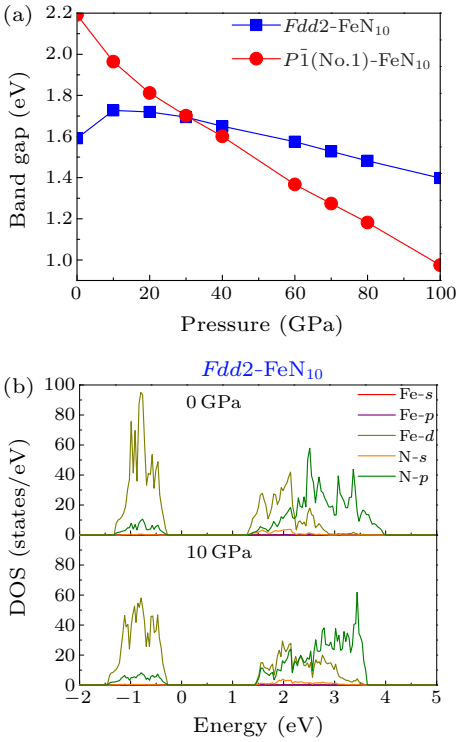

Fig. 7. (a) Pressure dependence of electronic band gaps. (b) Partial density of states of $Fdd2$-FeN_{10} at 0 GPa and 10 GPa, respectively.

Table 1. Detonation properties of $Fdd2$-FeN_{10} and $P\bar{1}$(No.1)-FeN_{10}. The reported values of TNT and HMX serve as a comparison. The results are calculated with the Kamlet–Jacobs equations.

Compounds	E_d (kJ/g)	ρ (g/cm^3)	D (km/s)	P (kbar)
$Fdd2$-FeN_{10}	3.709	3.211	14.220	1189.372
$P\bar{1}$(No.1)-FeN_{10}	6.349	2.197	12.119	728.108
TNT	4.30	1.64	6.90	190
HMX	5.70	1.90	9.10	393

In summary, through the combination of first-principles calculations and a molecular crystal search method, we find two new iron pentazolate salts, namely $Fdd2$-FeN_{10} and $P\bar{1}$(No.1)-FeN_{10}. The energy density (3.709 kJ/g) of $Fdd2$-FeN_{10} with the lowest enthalpy is close to TNT, while the energy density of $P\bar{1}$(No.1)-FeN_{10} is as high as 6.349 kJ/g, which exceeds that of HMX. Formation enthalpy and phonon spectrum indicate the thermodynamic and mechanical stability of $Fdd2$-FeN_{10} and $P\bar{1}$(No.1)-FeN_{10}, and $Fdd2$-FeN_{10} may have a relatively low synthesis pressure (∼20 GPa). AIMD simulations demonstrate that the two compounds can maintain stable within 10 ps under ambient conditions. Meanwhile, the research of electronic properties reveals semiconducting and insulating behavior of $Fdd2$-FeN_{10} and $P\bar{1}$(No.1)-FeN_{10}. In addition, $Fdd2$-FeN_{10} and $P\bar{1}$(No.1)-FeN_{10} also show good explosive performance, indicating their potential application prospects in the field of high-energy explosions. This work not only predicts a more stable dehydrated iron pentazolate salt, but also explores the crystal structure of iron bispentazole, providing a reference for subsequent experimental and theoretical works.

Acknowledgments. This work was supported by the National Natural Science Foundation of China (Grant No. 51971037), and the National Key Research and Development Program of China (Grant No. 2017YFB0701603). We gratefully acknowledge HZWTECH for providing computation facilities.

References

[1] Xu Y, Wang Q, Shen C, Lin Q, Wang P and Lu M 2017 *Nature* **549** 78
[2] Zhang C, Sun C, Hu B, Yu C and Lu M 2017 *Science* **355** 374
[3] Zhang C, Yang C, Hu B, Yu C, Zheng Z and Sun C 2017 *Angew. Chem. Int. Ed.* **56** 4512
[4] Luo J H, Chen L Y, Nguyen D N, Guo D, An Q and Cheng M J 2018 *J. Phys. Chem. C* **122** 21192
[5] Peng F, Yao Y, Liu H and Ma Y 2015 *J. Phys. Chem. Lett.* **6** 2363
[6] Steele B A and Oleynik I I 2016 *Chem. Phys. Lett.* **643** 21
[7] Steele B A, Stavrou E, Crowhurst J C, Zaug J M, Prakapenka V B and Oleynik I I 2017 *Chem. Mater.* **29** 735
[8] Laniel D, Weck G, Gaiffe G, Garbarino G and Loubeyre P 2018 *J. Phys. Chem. Lett.* **9** 1600
[9] Li J, Sun L, Wang X, Zhu H and Miao M 2018 *J. Phys. Chem. C* **122** 22339
[10] Xia K, Yuan J, Zheng X, Liu C, Gao H, Wu Q and Sun J 2019 *J. Phys. Chem. Lett.* **10** 6166
[11] Xia K, Zheng X, Yuan J, Liu C, Gao H, Wu Q and Sun J 2019 *J. Phys. Chem. C* **123** 10205
[12] Liu Z, Li D, Tian F, Duan D, Li H and Cui T 2020 *Inorg. Chem.* **59** 8002
[13] Yi W C, Zhao K F, Wang Z X, Yang B C, Liu Z and Liu X B 2020 *ACS Omega* **5** 6221
[14] Yi W, Zhao L, Liu X, Chen X, Zheng Y and Miao M 2020 *Mater. & Des.* **193** 108820
[15] Yuan J N, Xia K, Wu J F and Sun J 2021 *Sci. Chin. Phys. Mech. & Astron.* **64** 218211
[16] Wang Y, Lv J, Zhu L and Ma Y 2010 *Phys. Rev. B* **82** 094116
[17] Wang Y, Lv J, Zhu L and Ma Y 2012 *Comput. Phys. Commun.* **183** 2063
[18] Wang H, Wang Y, Lv J, Li Q, Zhang L and Ma Y 2016 *Comput. Mater. Sci.* **112** 406
[19] Kresse G and Furthmüller J 1996 *Phys. Rev. B* **54** 11169
[20] Perdew J P, Burke K and Ernzerhof M 1996 *Phys. Rev. Lett.* **77** 3865
[21] Blöchl P E 1994 *Phys. Rev. B* **50** 17953
[22] Grimme S, Ehrlich S and Goerigk L 2011 *J. Comput. Chem.* **32** 1456
[23] Klimeš J, Bowler D R and Michaelides A 2010 *J. Phys.: Condens. Matter* **22** 022201
[24] Togo A and Tanaka I 2015 *Scr. Mater.* **108** 1
[25] Pickard C J and Needs R J 2009 *Phys. Rev. Lett.* **102** 125702
[26] Jiao F, Zhang C and Xie W 2020 *J. Phys. Chem. C* **124** 19953
[27] Suzuki K, Morita H, Kaneko T, Yoshida H and Fujimori H 1993 *J. Alloys Compd.* **201** 11
[28] Zhang J, Oganov A R, Li X and Niu H 2017 *Phys. Rev. B* **95** 020103
[29] Huang B, Wang B, Wu S, Guégan F, Hu W and Frapper G 2021 *Chem. Mater.* **33** 5298
[30] Huang S D, Shang C, Kang P L, Zhang X J and Liu Z P 2019 *WWIREs: Comput. Mol. Sci.* **9** e1415
[31] Shang C, Zhang X J and Liu Z P 2014 *Phys. Chem. Chem. Phys.* **16** 17845
[32] Yi W C, Jiang X G, Yang T, Yang B C, Liu Z and Liu X B 2020 *ACS Omega* **5** 24946
[33] Zhang X, Yang J, Lu M and Gong X 2015 *Struct. Chem.* **26** 785
[34] Wozniak D R and Piercey D G 2020 *Engineering* **6** 981
[35] Lein M, Frunzke J, Timoshkin A and Frenking G 2001 *Chem. Eur. J.* **7** 4155
[36] Frenking G 2001 *J. Organomet. Chem.* **635** 9
[37] Sanville E, Kenny S D, Smith R and Henkelman G 2007 *J. Comput. Chem.* **28** 899
[38] Deringer V L, Tchougréeff A L and Dronskowski R 2011 *J. Phys. Chem. A* **115** 5461
[39] Maintz S, Deringer V L and Tchougréeff A L 2016 *J. Comput. Chem.* **37** 1030
[40] Hedin L 1965 *Phys. Rev.* **139** A796
[41] Shishkin M and Kresse G 2007 *Phys. Rev. B* **75** 235102
[42] Luo W D, Ismail-Beigi S, Cohen M L and Louie S G 2002 *Phys. Rev. B* **66** 195215
[43] Liu L, Zhang S and Zhang H 2022 *Chin. Phys. Lett.* **39** 056102
[44] Kamlet M J and Dickinson C 1968 *J. Chem. Phys.* **48** 43

Supplemental Material: Predicted Pressure-Induced High-Energy-Density Iron Pentazolate Salts

Chuli Sun (孙矗丽)[2], Wei Guo (郭伟)[1,2,3*], and Yugui Yao (姚裕贵)[1,2,3]

[1]*Frontiers Science Center for High Energy Material (MOE), Beijing Institute of Technology, Beijing 100081, China*

[2]*Key Laboratory of Advanced Optoelectronic Quantum Architecture and Measurement (MOE), School of Physics, Beijing Institute of Technology, Beijing 100081, People's Republic of China*

[3]*State Key Laboratory of Explosion Science and Technology, Beijing Institute of Technology, Beijing 100081, China*

Table S1: The lattice parameters and atomic positions of *Fdd*2-FeN_{10}, *P*-1(No.1)-FeN_{10} and *P*-1(No.2)-FeN_{10} under ambient pressure.

Space group	Lattice parameters	Atomic coordinates (fractional)
*Fdd*2	a=10.748, b=8.910, c=8.463 α=90.0, β=90.0, γ=90.0	Fe (0.500, 0.500, 0.271) N (0.372, 0.923, 0.246) (0.257, 0.082, 0.364) (0.507, 0.346, 0.443) (0.683, 0.001, 0.769) (0.122, 0.220, 0.099)
P-1(No.1)	a=5.229, b=5.373, c=6.687 α=91.322, β=110.802, γ=119.586	Fe (0.000, 0.000, 0.000) N (0.181, 0.924, 0.294) (0.302, 0.370, 0.243) (0.598, 0.981, 0.798) (0.880, 0.859, 0.681) (0.524, 0.706, 0.829)
P-1(No.2)	a=3.959, b=3.961, c=7.201 α=96.630, β=103.731, γ=99.842	Fe (0.000, 0.500, 0.000) N (0.644, 0.775, 0.898) (0.435, 0.076, 0.681) (0.705, 0.355, 0.179) (0.284, 0.934, 0.177) (0.823, 0.183, 0.320)

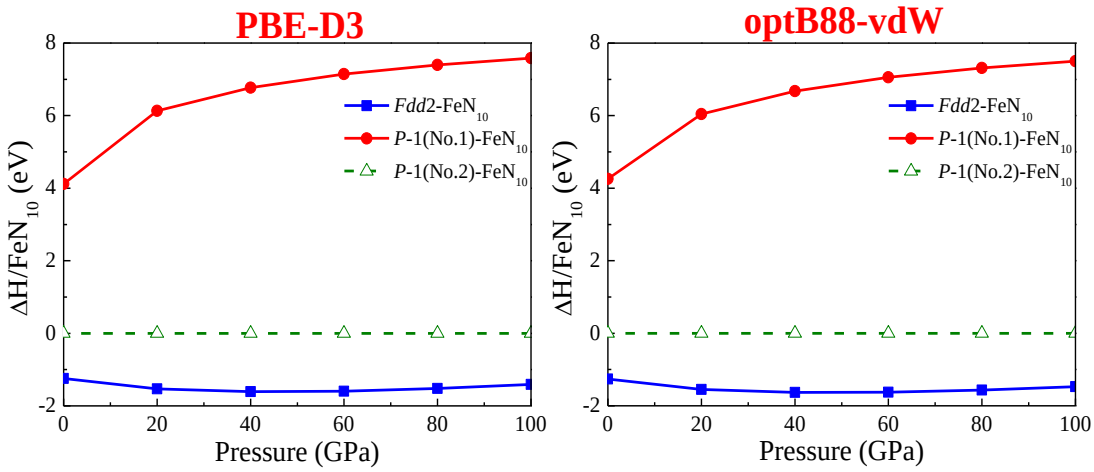

Figure S1: Relative enthalpies of *Fdd*2-FeN_{10}, *P*-1(No.1)-FeN_{10} and *P*-1(No.2)-FeN_{10} under different van der Waals correction methods (PBE-D3 and optB88-vdW). The enthalpy of *P*-1(No.2)-FeN_{10} is used as the reference state.

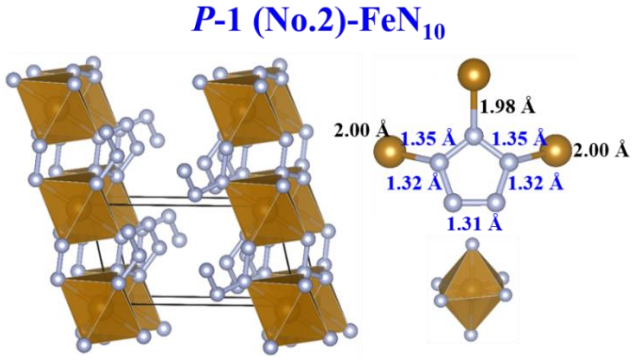

Figure S2: The crystal structure and bond lengths (Fe-N: black, N-N: blue) of *P*-1(No.2)-FeN_{10} at 0 GPa.

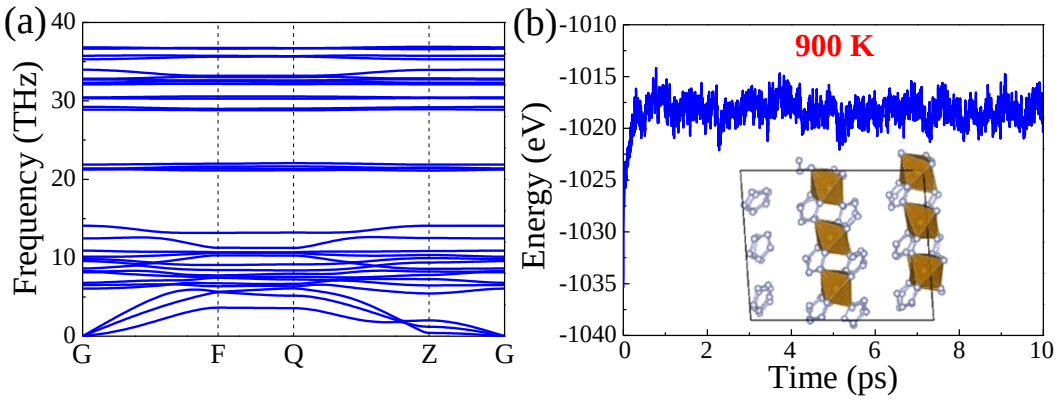

Figure S3: (a) Phonon dispersion curves *P*-1(No.2)-FeN_{10} at 0 GPa. (b) Total free energy fluctuations of *P*-1(No.2)-FeN_{10} at 900 K under ambient pressure. The illustration shows structural snapshots of *P*-1(No.2)-FeN_{10} after 10 ps in AIMD simulations.

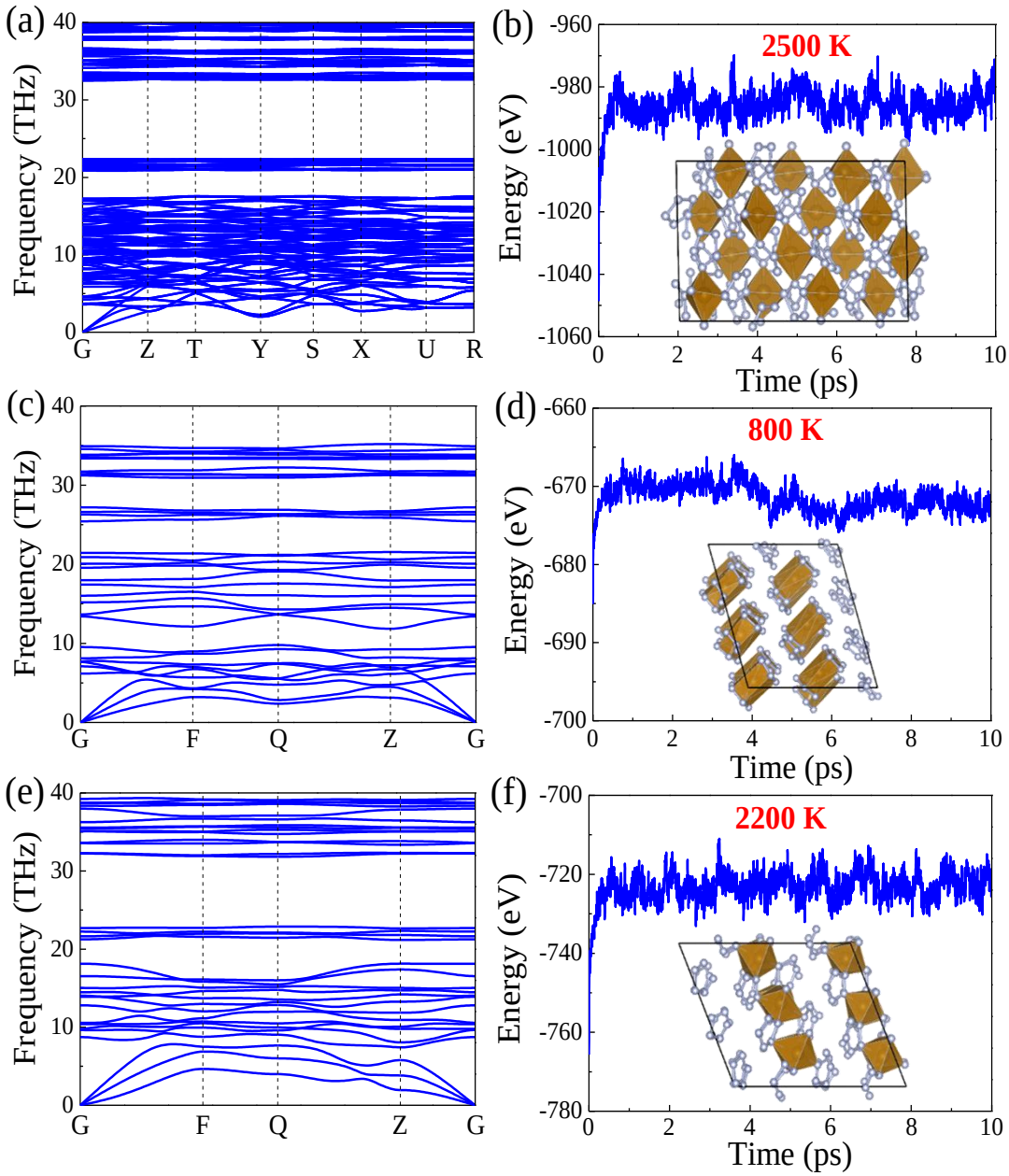

Figure S4: (a) (c) (e) Phonon dispersion curves of *Fdd*2-FeN_{10}, *P*-1(No.1)-FeN_{10} and *P*-1(No.2)-FeN_{10} at 40 GPa. (b) (d) (f) Total free energy fluctuations of *Fdd*2-FeN_{10}, *P*-1(No.1)-FeN_{10} and *P*-1(No.2)-FeN_{10} in AIMD simulations. 2500 K, 800 K and 2200 K are the highest temperature at which *Fdd*2-FeN_{10}, *P*-1(No.1)-FeN_{10} and *P*-1(No.2)-FeN_{10} can remain stable at 40 GPa respectively, and the illustrations show their structural snapshots after 10 ps.

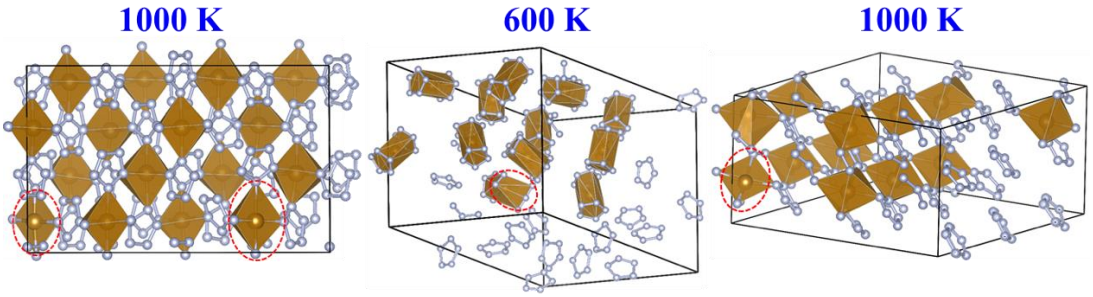

Figure S5: Temperatures and snapshots of *Fdd*2-FeN_{10}, *P*-1(No.1)-FeN_{10} and *P*-1(No.2)-FeN_{10} losing stability in AIMD simulations under ambient pressure.

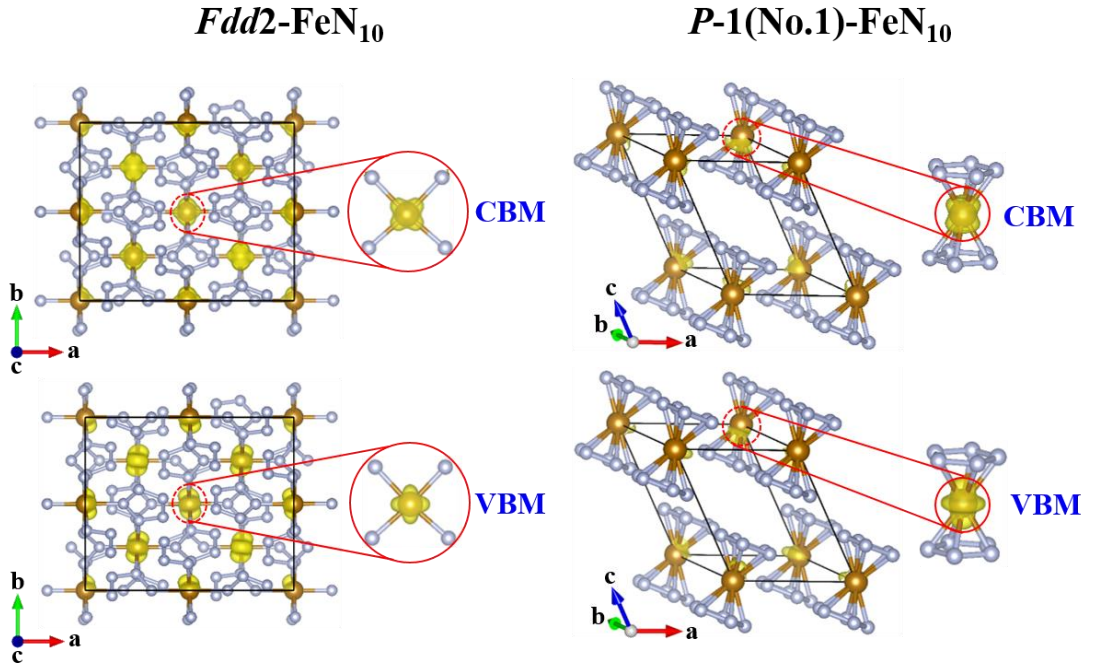

Figure S6: The partial charges of *Fdd*2-FeN_{10} and *P*-1(No.1)-FeN_{10} at ambient pressure.

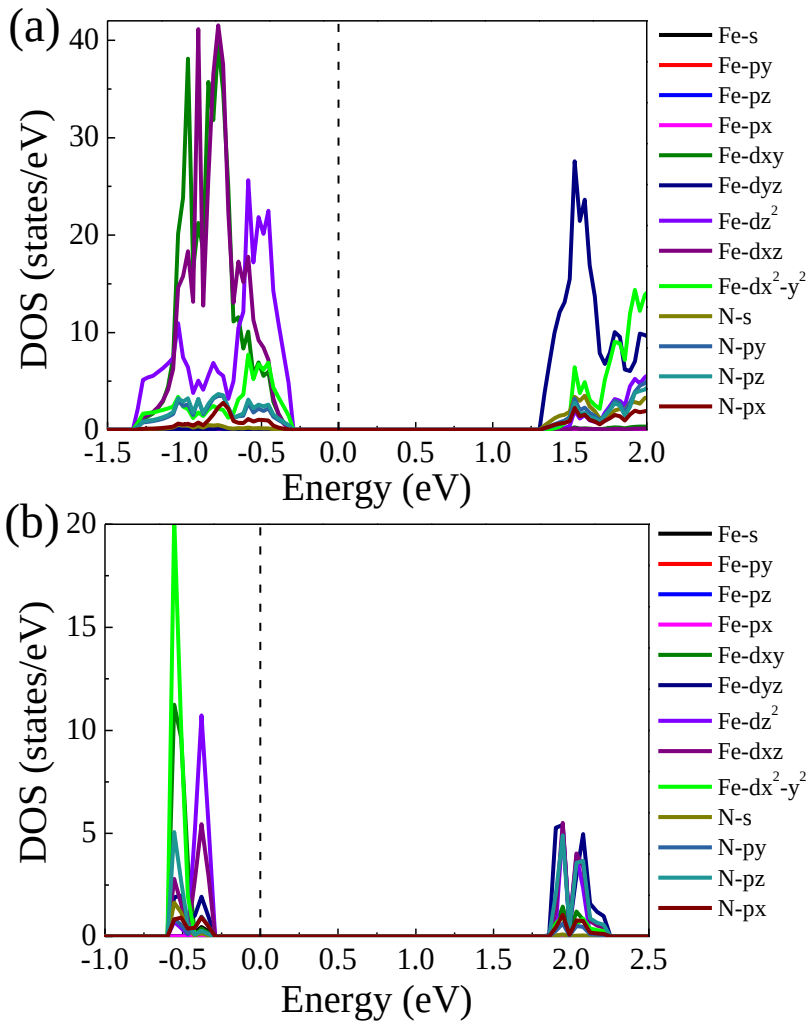

Figure S7: Partial density of states of *Fdd*2-FeN_{10} and *P*-1(No.1)-FeN_{10} at 0 GPa.

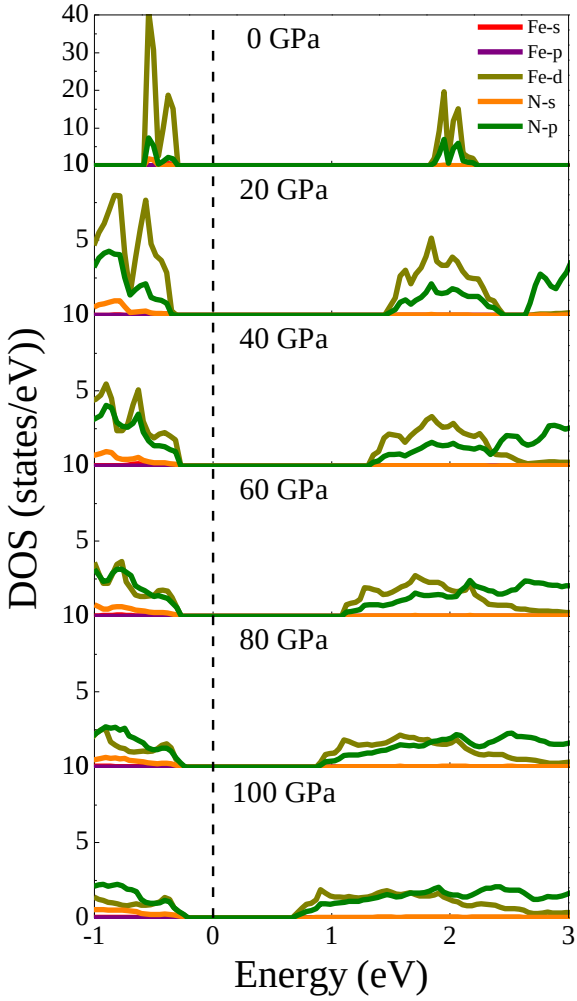

Figure S8: Partial density of states of *P*-1(No.1)-FeN_{10} at 0-100 GPa.

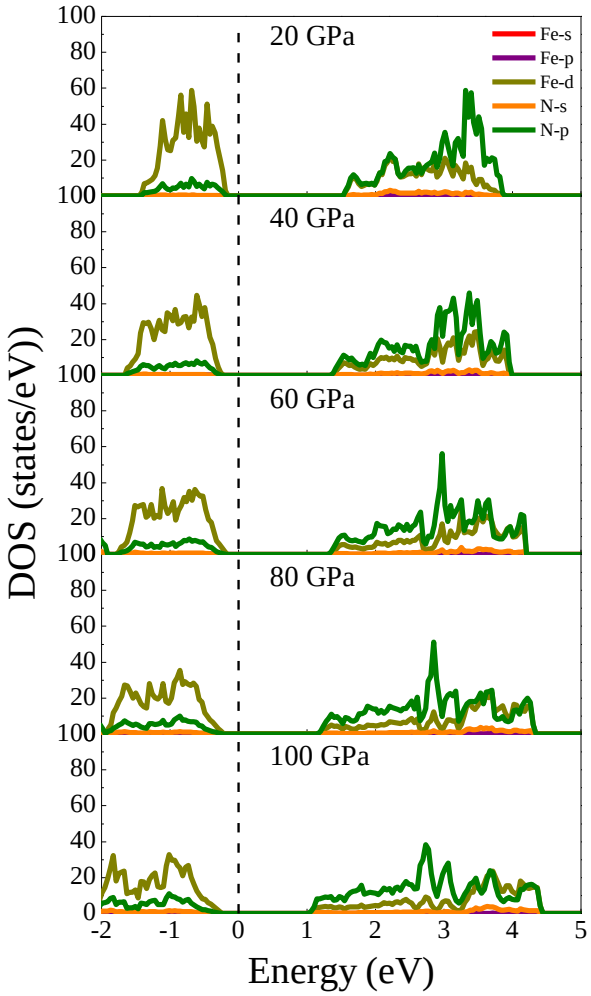

Figure S9: Partial density of states of *Fdd*2-FeN_{10} above 10 GPa.